arXiv:1304.2164v1 [astro-ph.CO] 8 Apr 2013

Effect of Mask Regions on Weak Lensing Statistics

Masato Shirasaki

Department of Physics, University of Tokyo, Tokyo 113-0033, Japan

`masato.shirasaki@utap.phys.s.u-tokyo.ac.jp`

Naoki Yoshida

Department of Physics, University of Tokyo, Tokyo 113-0033, Japan
Kavli Institute for the Physics and Mathematics of the Universe, University of Tokyo, Kashiwa, Chiba 277-8583, Japan

and

Takashi Hamana

National Astronomical Observatory of Japan, Tokyo 181-0015, Japan

ABSTRACT

Sky masking is unavoidable in wide-field weak lensing observations. We study how masks affect the measurement of statistics of matter distribution probed by weak gravitational lensing. We first use 1000 Gaussian simulations in order to examine in detail the impact of mask regions on the weak lensing Minkowski Functionals (MFs). We consider actual sky masks used for a Subaru Suprime-Cam imaging survey. The masks increase the variance of the convergence field and thus the expected values of the MFs are biased even for a Gaussian random field. The bias is caused by two effects. One is owing to the reduced number of sampling Fourier modes, which can be accounted for analytically by considering the survey geometry appropriately. The other is owing to variation of the variance of the convergence field for each field of view. Lensing MFs are biased systematically when the reconstructed convergence field is normalized by its variance. We then use a large number of cosmological ray-tracing simulations in order to address if the lensing MFs measured for a Subaru 2-deg^2 survey are consistent with those of the standard cosmology. The resulting $\chi^2/n_{\rm dof} = 29.6/30$ for combined three MFs, obtained by taking the mask effects into account, suggests that the observational data are indeed consistent with the standard ΛCDM model. Finally, we explore how masked covariance matrices affect cosmological parameter estimation. We conclude that the lensing MFs are powerful probe of cosmology only if the effect of masking is correctly taken into account.

1. INTRODUCTION

An array of recent observations such as the cosmic microwave background (CMB) anisotropies (e.g. Komatsu et al. 2011; Planck Collaboration et al. 2013) and the large-scale structure (e.g. Tegmark et al. 2006; Reid et al. 2010) established the standard ΛCDM model. The energy content of the present-day universe is dominated by dark energy and dark matter, and the primordial density fluctuations, that seeded all rich structure we observe today, were generated through inflation in the very early universe. There still remain a few important questions such as the nature of dark energy, the physical properties of dark matter, and the exact mechanism that generates the primordial density fluctuations.

Gravitational lensing is a powerful method to study matter distribution (e.g. Oguri et al. 2012). Future weak lensing surveys are aimed at measuring cosmic shear over a wide area of more than a thousand square degrees. Such observational programmes include Subaru Hyper Suprime-Cam (HSC) [1], the Dark Energy Survey (DES) [2], and the Large Synoptic Survey Telescope (LSST) [3]. Space missions such as Euclid and WFIRST are also promising. The large set of cosmic shear data will enable us to improve the constraints on cosmological parameters which provides important clues to the mysterious dark components.

A variety of statistics are proposed to characterize the large-scale matter distribution. Minkowski Functionals (MFs) are among the most useful statistics to extract non-Gaussian informations from a two-dimensional or three-dimensional field. For example, MFs have been applied to the observed CMB maps and provided comparable constraints to those obtained using the CMB bispectrum (Hikage et al. 2008). Matsubara & Jain (2001) and Sato et al. (2001) studied Ω_m-dependence of weak lensing MFs. More recently, Kratochvil et al. (2012) showed that the lensing MFs contain significant cosmological information, beyond the power-spectrum, whereas Shirasaki et al. (2012) showed that weak lensing MFs can be used to constrain the statistical properties of the primordial density fluctuations.

These previous studies on weak lensing MFs consider often idealized cases. There exist, however, many observational effects in real weak lensing measurement. For example, imperfect shape measurement due to seeing and optical distortion, selection effects of galaxies, uncertain redshift distribution of galaxies due to photometric redshift error (e.g. Bolzonella et al. 2000), noise-rectification biases (e.g. Kaiser 2000; Erben et al. 2001; Hirata & Seljak 2003), and complicated survey geometry due to mask regions. Some of these effects on cosmic shear power spectrum analysis have been already studied (e.g. Huterer et al. 2006; Hikage et al. 2011). A comprehensive study of observational effects on lensing MFs are also needed in order to fully exploit the data from

---

[1] http://www.naoj.org/Projects/HSC/j_index.html

[2] http://www.darkenergysurvey.org/

[3] http://www.lsst.org/lsst/

upcoming wide cosmology surveys.

In the present paper, we study the impact of mask regions on measurement of weak lensing MFs. Masking effect can be one of the major systematics because MFs are intrinsically morphological quantities. We use a large set of numerical simulations to critically examine the effect of masking. We then directly measure the lensing MFs from real observational data obtained from a Subaru survey. We compare the observed MFs with the results of our ray-tracing simulations that include the effect of mask regions explicitly.

The rest of the present paper is organized as follows. In Section 2, we summarize the basics of MFs and how to estimate MFs from observed shear field. In Section 3, we describe the data used in this paper and the details of numerical simulations which includes ray-tracing simulations of gravitational lensing. In Section 4, we show the results of the impact of mask regions on lensing MFs. We also represent the comparison with observed MFs and ray-tracing simulation results. We then perform the simple analysis to characterize the impact of mask regions on cosmological constraints from lensing MFs. Concluding remarks and discussions are given in Section 5.

2. MINKOWSKI FUNCTIONALS

2.1. Basics

Minkowski Functionals (MFs) are morphological statistics for some smoothed random field above a certain threshold. In general, for a given D-dimensional smoothed field $\mathbb{S}^D$, one can calculate $D+1$ MFs V_i. On $\mathbb{S}^2$, one can thus define 2+1 MFs V_0, V_1 and V_2. For a given threshold, V_0, V_1 and V_2 describe the fraction of area, the total boundary length of contours, and the integral of the geodesic curvature K along the contours, respectively. MFs are defined, for threshold ν, as

$$V_0(\nu) \equiv \frac{1}{4\pi} \int_{Q_\nu} \mathrm{d}S, \tag{1}$$

$$V_1(\nu) \equiv \frac{1}{4\pi} \int_{\partial Q_\nu} \frac{1}{4} \mathrm{d}\ell, \tag{2}$$

$$V_2(\nu) \equiv \frac{1}{4\pi} \int_{\partial Q_\nu} \frac{1}{2\pi} K \mathrm{d}\ell, \tag{3}$$

where Q_ν and ∂Q_ν represent the excursion set and the boundary of the excursion set for a smoothed field $u(\boldsymbol{\theta})$. They are given by

$$Q_\nu = \{\boldsymbol{\theta} \,|\, u(\boldsymbol{\theta}) > \nu\}, \tag{4}$$

$$\partial Q_\nu = \{\boldsymbol{\theta} \,|\, u(\boldsymbol{\theta}) = \nu\}. \tag{5}$$

For a two-dimensional Gaussian random field, one can calculate the expectation values for MFs analytically (Tomita 1986):

$$V_0(\nu) = \frac{1}{2} \left[1 - \mathrm{erf}\left(\frac{\nu - \mu}{\sigma_0} \right) \right], \tag{6}$$

$$V_1(\nu) \;=\; \frac{1}{8\sqrt{2}}\frac{\sigma_1}{\sigma_0}\exp\left(-\frac{(\nu-\mu)^2}{\sigma_0^2}\right), \tag{7}$$

$$V_2(\nu) \;=\; \frac{\nu-\mu}{2(2\pi)^{3/2}}\frac{\sigma_1^2}{\sigma_0^3}\exp\left(-\frac{(\nu-\mu)^2}{\sigma_0^2}\right), \tag{8}$$

where $\mu = \langle u\rangle$, $\sigma_0^2 = \langle u^2\rangle - \mu^2$, and $\sigma_1^2 = \langle|\nabla u|^2\rangle$.

2.2. Estimation of Lensing MFs from Cosmic Shear Data

We summarize how to estimate lensing MFs from observed shear data. Let us first define the weak lensing mass maps which corresponds to the smoothed lensing convergence field κ:

$$\mathcal{K}(\boldsymbol{\theta}) = \int \mathrm{d}^2\phi\; \kappa(\boldsymbol{\theta}-\boldsymbol{\phi})U(\boldsymbol{\phi}), \tag{9}$$

where U is the filter function to be specified below. We can calculate the same quantity by smoothing the shear field γ as

$$\mathcal{K}(\boldsymbol{\theta}) = \int \mathrm{d}^2\phi\; \gamma_t(\boldsymbol{\phi}:\boldsymbol{\theta})Q_t(\boldsymbol{\phi}), \tag{10}$$

where γ_t is the tangential component of the shear at position $\boldsymbol{\phi}$ relative to the point $\boldsymbol{\theta}$. The filter function for the shear field Q_t relates to U by

$$Q_t(\theta) = \int_0^\theta \mathrm{d}\theta'\; \theta'U(\theta') - U(\theta). \tag{11}$$

We consider that Q_t is defined with a finite extent. In this case, one finds

$$U(\theta) = 2\int_\theta^{\theta_o} \mathrm{d}\theta'\; \frac{Q_t(\theta')}{\theta'} - Q_t(\theta), \tag{12}$$

where θ_o is the outer boundary of the filter function.

In the following, we consider the truncated Gaussian filter (for U) as

$$U(\theta) \;=\; \frac{1}{\pi\theta_G^2}\exp\left(-\frac{\theta^2}{\theta_G^2}\right) - \frac{1}{\pi\theta_o^2}\left(1-\exp\left(-\frac{\theta_o^2}{\theta_G^2}\right)\right), \tag{13}$$

$$Q_t(\theta) \;=\; \frac{1}{\pi\theta^2}\left[1-\left(1+\frac{\theta^2}{\theta_G^2}\right)\exp\left(-\frac{\theta^2}{\theta_G^2}\right)\right], \tag{14}$$

for $\theta \leq \theta_o$ and $U = Q_t = 0$ elsewhere. Throughout the present paper, we adopt $\theta_G = 1'$ and $\theta_o = 15'$. Note that this choice of θ_G corresponds to an optimal smoothing scale for detection of massive galaxy clusters using weak lensing with $z_{\mathrm{source}} = 1.0$ (Hamana et al. 2004).

We follow Lim & Simon (2012) to calculate the MFs from pixelated $\mathcal{K}$ maps. We convert a weak lensing field $\mathcal{K}$ to $x = (\mathcal{K} - \langle\mathcal{K}\rangle)/\sigma_0$ where σ_0 is the standard deviation of a weak lensing field

on a map. In binning the thresholds, we set $\Delta x = 0.2$ from $x = -5$ to $x = 5$. We have checked that the binning is sufficient to reproduce the analytic MFs formula (Tomita 1986) for 1000 maps of Gaussian random fields on a $5° \times 5°$ map without mask. When we estimate lensing MFs on a $\mathcal{K}$ map with mask, we discard the pixels within $2\theta_G$ from the mask boundaries, because $\mathcal{K}$ data on such regions are affected by the lack of shear data.

3. DATA

3.1. Suprime-Cam

We use the i'-band data from the Subaru/Suprime-Cam data archive SMOKA[1]. The observation is characterized as follows. The area is contiguous with at least four pointings, the exposure time for each pointing is longer than 1800 sec, and the seeing full width at half-maximum (FWHM) is better than 0.65 arcsec. The data is dubbed "COSMOS" in Table A1 in Hamana et al. (2012).

We conservatively use the data only within 15 arcmin radius from the field center of Suprime-Cam, because the point spread function (PSF) becomes elongated significantly outside of the central area, which may make PSF correction inaccurate. Then mosaic stacking is performed with SCAMP (Bertin 2006) and SWarp (Bertin et al. 2002). We use SExtractor (Bertin & Arnouts 1996) and $hfindpeaks$ of IMCAT software (Kaiser et al. 1995), and then the two catalogues are merged by matching positions of the detected objects with a tolerance of 1 arcsec.

For weak lensing analysis, we follow the KSB method (Kaiser et al. 1995; Luppino & Kaiser 1997; Hoekstra et al. 1998). Stars are selected in the standard way by identifying the appropriate branch in the magnitude half-light radius (rh) plane, along with the detection significance cut $S/N > 10$. We found that the number density of stars is ~ 1 arcmin^{-2}. We use the galaxy images that satisfy the following three conditions; (i) the detection significance of $S/N > 3$ and $\nu > 10$ where ν is an estimate of the peak significance given by $hfindpeaks$, (ii) rh is larger than the stellar branch, and (iii) the AB magnitude is in the range of $22 < i' < 25$ (where MAG_AUTO given by the SExtractor is used for the magnitude and slightly different from Hamana et al. (2012)). The resulting number density of galaxies n_{gal} is then 15.8 arcmin^{-2}. We measure the shapes of the objects by $getshapes$ of IMCAT, and correct for the PSF by the KSB method. The rms of the galaxy ellipticities after the PSF correction is 0.314.

Next, we define data and mask regions by using the observed positions of the source galaxies as follows. We map the observation area onto rectangular pixels of width 0.15 arcmin. For each pixel, we check if there is a galaxy within $\theta_D = 0.4$ arcmin from the pixel center. If there are no galaxies, then the pixel is marked as a mask pixel. After performing the procedure for all the pixels, the marked pixels are masked regions, whereas the other pixels are data regions. However,

---
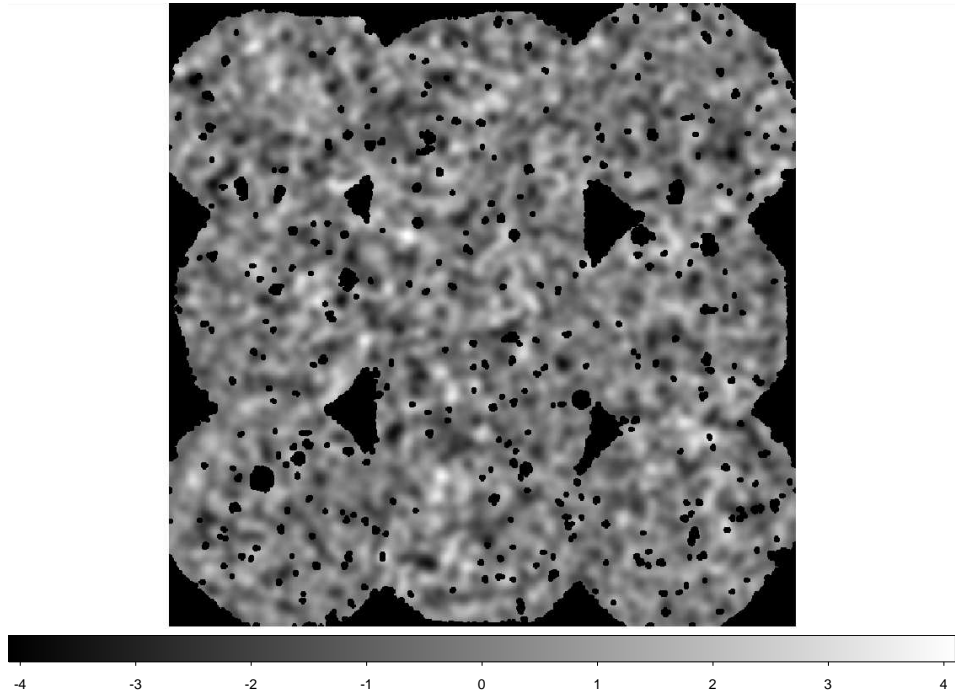
[1]http://smoka.nao.ac.jp/

Fig. 1.— The reconstructed lensing field $\mathcal{K}$ from the Subaru Suprime-Cam data. The convergence $\mathcal{K}$ is computed from the ellipticity of 102342 source galaxies by Eq.(10). The masked survey area (black portion) covers 0.34 deg^2. The grey-scale bar shows the value of $(\mathcal{K} - \langle \mathcal{K} \rangle)/\sigma_0$.

we unmask "isolated" masked pixels whose surrounding pixels are all data pixels.

Weak lensing convergence field $\mathcal{K}$ is computed from the galaxy ellipticity data as in Eq. (10) on regular grids with a grid spacing of 0.15 arcmin. The resulting mass map includes mask regions as shown in Figure 1. The masked regions cover 0.34 deg^2 in total. The unmasked regions are found to be 1.79 deg^2. Note that we use only 0.575 deg^2 in unmasked regions for lensing MFs analysis because we remove the ill-defined pixels within $2\theta_G = 2$ arcmin from the boundary of mask.

3.2. Gaussian and Ray-tracing Simulation

We first use 1000 Gaussian convergence maps to study the impact of mask regions on the lensing MFs. We generate the maps for our fiducial cosmology using the fitting formula of Smith et al. (2003) to calculate the matter power spectrum $P(k; z)$. We then integrate the matter power spectrum over redshift z, convolved with a weighting function for the source redshift $z_{\text{source}} = 1$. Each convergence map is defined on 2048^2 grid points with an angular grid size of 0.15 arcmin.

In addition to the Gaussian simulations, we use 1000 ray-tracing simulations of weak gravitational lensing of Sato et al. (2009) [1]. The ray-tracing simulations are performed on light-cone outputs that are generated by arranging multiple simulation boxes. Briefly, small- and large-volume N-body simulations are placed to cover a past light-cone of a hypothetical observer with an angular extent $5° \times 5°$, from redshift $z = 0$ to $z = 3.5$, similarly to the methods in White & Hu (2000) and Hamana & Mellier (2001). We set the source redshift $z_{\rm source} = 1$ for the ray-tracing simulations. The grid size and hence the angular resolution are kept the same as our Gaussian simulations described above. Details of the ray-tracing simulations are found in Sato et al. (2009).

It is well-known that the intrinsic ellipiticities of source galaxies induce noises to lensing shear maps. We model the noise by adding random ellipiticities drawn from a two-dimensional Gaussian to the simulated shear data. We set the root-mean-square of intrinsic ellipiticities to be 0.314 and the number of source galaxies is set 15.8 arcmin^{-2}. The values are obtained from the actual weak lensing observations described in Section 3.1.

4. RESULT

4.1. Masking Effect on MFs: Gaussian Fields

We first discuss the effect of masking on the lensing MFs. We calculate the MFs for 1000 Gaussian convergence maps with and without mask. Figure 2 compares the results for V_0, V_1, and V_2. In each upper panel, the black points are the results with mask whereas the gray points are for those without mask. The error bars show the standard deviation of the MFs measured from our 1000 maps. We also plot the difference between the masked maps and the unmasked maps in the lower panel. Clearly the expected values of the MFs are biased with the mask. The amplitude of the bias corresponds to approximately 5 percent differences of the variance amplitude (see Appendix A).

It is important to study the effects of mask regions in a more quantitative manner. The variance of the MFs in each bin is larger for the masked maps, because the number of pixels used to evaluate the MFs is effectively reduced by the mask. We can approximately evaluate the increase of variance by scaling the effective survey area. The bias of weak lensing MFs is actually caused by two distinct effects. One is owing to the reduced number of sampling Fourier modes in a $\mathcal{K}$ field because of the mask. This changes the amplitude of MFs because both $\sigma_0^2 = \langle (\mathcal{K} - \langle \mathcal{K} \rangle)^2 \rangle$ and $\sigma_1^2 = \langle |\nabla \mathcal{K}|^2 \rangle$ get smaller. We find that the differences of the MFs between the masked Gaussian maps and the unmasked ones are indeed explained by systematic decrease in σ_0 and σ_1 (see Appendix A for details). Another effect is caused by variation of the variance σ_0 among different fields of view. In order to calculate the lensing MFs in real observations, we need to normalize the reconstructed

---

[1] For the simulations, the adopted cosmology is consistent with WMAP3 year results (Spergel et al. 2007).
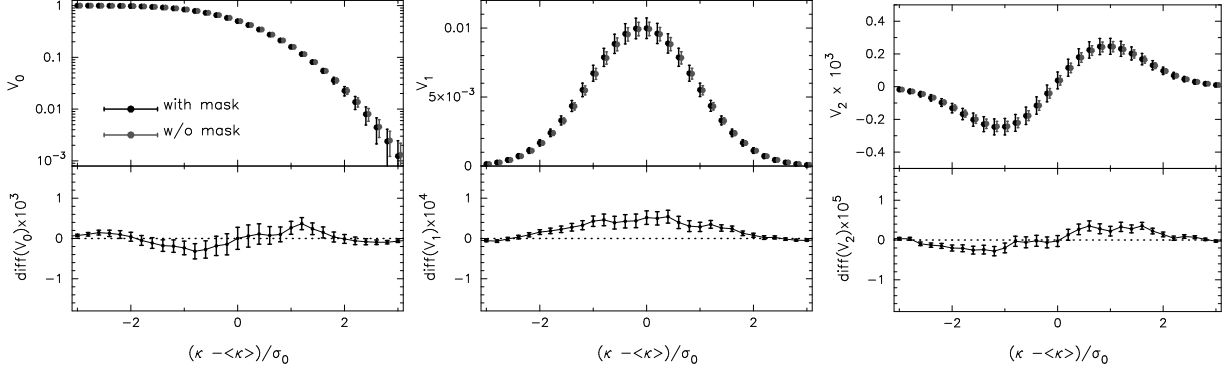
Fig. 2.— Masking effect on the lensing MFs. In the upper panel, the black points with error bars show the MFs with mask whereas the grey points are the results without mask. The lower panels show the differences of MFs between the masked and unmasked maps. We use 1000 Gaussian convergence maps with Gaussian smoothing with a length scale of 1 arcmin. The error bars in the lower panel indicate the standard deviation estimated from the 1000 maps.

lensing convergence field by its variance. The normalization then causes fluctuations of the MFs from expected values because the MFs are defined as a function of $x = (\mathcal{K} - \langle\mathcal{K}\rangle)/\sigma_0$ where σ_0 is evaluated for each field of view. The effect appears strong with masking because the variance σ_0 itself becomes smaller for masked maps than for unmasked maps. Unfortunately, it is difficult to calculate this effect analytically because the variance depends on a number of elements such as the exact geometry and the size distribution of the mask regions, and also on the smoothing scale etc. We thus resort to estimating the effect directly using a set of numerical simulations.

Figure 3 summarizes the effect of mask regions. There, we compare the mean of V_0 over 1000 Gaussian maps with the Gaussian prediction given by Eq. (6). For the Gaussian prediction, we estimate the quantities $\langle\mathcal{K}\rangle$, σ_0 and σ_1 from a total of 1000 realizations for masked and unmasked maps, respectively. These quantities thus serve as 'global' values. The error bars in each plot represent the variance of V_0 around the mean. The left and right panels differ in that the MFs are plotted as a function of $\mathcal{K} - \langle\mathcal{K}\rangle$ in the left panel whereas those in the right panel are shown as a function of $(\mathcal{K} - \langle\mathcal{K}\rangle)/\sigma_0$. Hence the apparent variance of the MFs (error bars) in the right panel includes somewhat artificial fluctuations due to the variance of the measured σ_0 for each field of view. In the lower panels, we show the difference between the mean V_0 and the Gaussian prediction. The difference should be compared with the field variance that are indicated by error bars. Notice that the difference from the Gaussian prediction is larger than the field variance when the MFs are evaluated with normalization as $(\mathcal{K} - \langle\mathcal{K}\rangle)/\sigma_0$. On the other hand, the Gaussian prediction describes well the mean MFs for both masked and unmasked maps as long as the MFs are evaluated *without* normalization of $\mathcal{K}$ by σ_0 (left panel). Clearly the systematic decrease of σ_0 and σ_1 due to mask regions introduce a significant bias to the MFs.
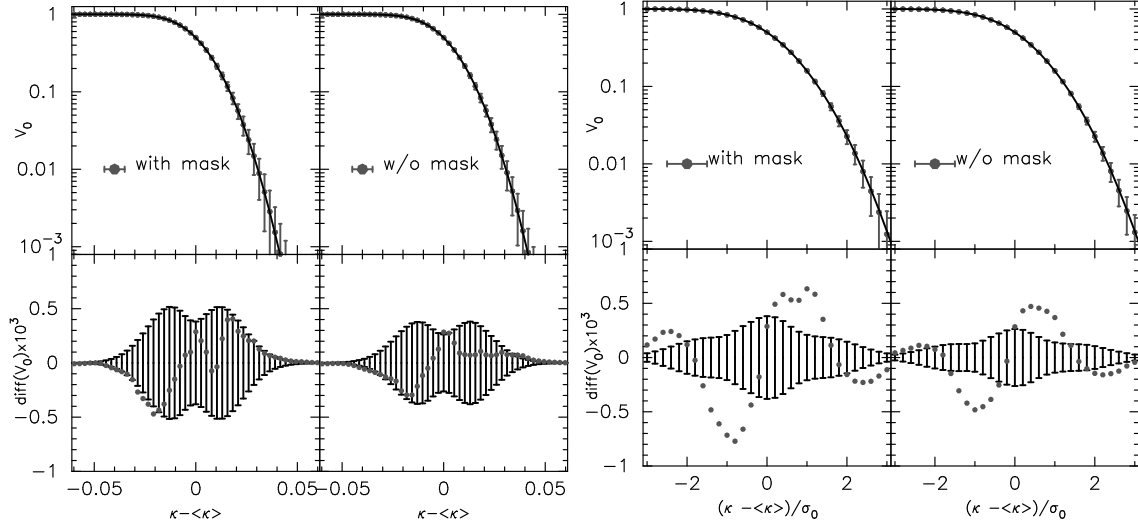
Fig. 3.— The effect of normalization of the MFs. We compare the mean V_0 over 1000 maps with the Gaussian prediction of Eq (6). In the right panel, V_0 in the left panel is calculated without normalization whereas that in the right panel is calculated for each $\mathcal{K}$ field normalized by its variance (see text and the horizontal axes label). The gray points in the lower portion show the differences between the mean V_0 and the Gaussian prediction. The differences are also compared with the variance of V_0 estimated from our 1000 maps (black error bars), i.e. the standard deviation of V_0 divided by $\sqrt{1000}$.

4.2. Ray-tracing lensing simulations

Having examined the effect of masking on Gaussian fields in the last section, we are now able to study the effect in more realistic cases. To this end, we use ray-tracing simulations of weak gravitational lensing described in Section 3.2. We pay particular attention to non-Gaussian features in the case with masks. The total non-Gaussianity probed by the lensing MFs $\Delta V_i^{\mathrm{obs}}$ is given by

$$\Delta V_i^{\mathrm{obs}} = V_i(\mathrm{masked}) - V_i^G(\mathrm{masked}), \tag{15}$$

where $V_i(\mathrm{masked})$ is i-th Minkowski Functional on a masked map and $V_i^G(\mathrm{masked})$ is the Gaussian term of $V_i(\mathrm{masked})$.

We can then decompose $\Delta V_i^{\mathrm{obs}}$ into three components:

$$\Delta V_i^{\mathrm{obs}} = \Delta V_i^{\mathrm{gravity}} + \Delta V_i^{\mathrm{bias}} - \Delta V_i^{\mathrm{bias,G}}, \tag{16}$$

$$\Delta V_i^{\mathrm{gravity}} = V_i(\mathrm{unmasked}) - V_i^G(\mathrm{unmasked}), \tag{17}$$

$$\Delta V_i^{\mathrm{bias}} = V_i(\mathrm{masked}) - V_i(\mathrm{unmasked}), \tag{18}$$

$$\Delta V_i^{\mathrm{bias,G}} = V_i^G(\mathrm{masked}) - V_i^G(\mathrm{unmasked}), \tag{19}$$
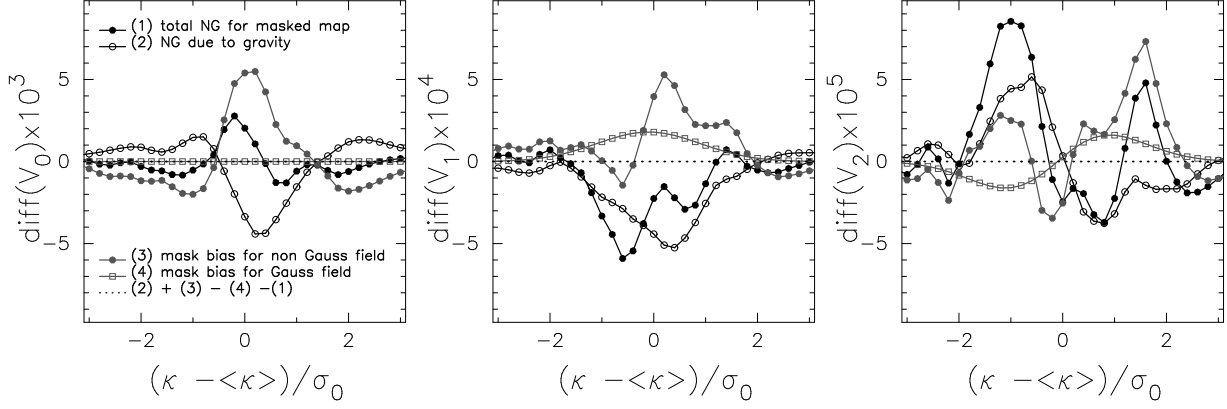
Fig. 4.— We plot the differences between the lensing MFs on masked ray-tracing simulation maps and the Gaussian term. The total non-Gaussianity obtained from the masked maps $\Delta V_i^{\mathrm{obs}}$ (black line with closed circle), the non-Gaussianity caused by non-linear gravitational growth $\Delta V_i^{\mathrm{gravity}}$ (black line with open circle), and the bias of lensing MFs due to mask regions for ray-tracing maps $\Delta V_i^{\mathrm{bias}}$ (gray line with closed circle). We also plot the Gaussian term of $\Delta V_i^{\mathrm{bias}}$ (gray line with open square). See the definition of each component given by Eq. (15)-(19).

where $\Delta V_i^{\mathrm{gravity}}$ represents the non-Gaussianity induced by non-linear gravitational growth, $\Delta V_i^{\mathrm{bias}}$ describes the mask bias of MFs for non-Gaussian maps, and $\Delta V_i^{\mathrm{bias,G}}$ corresponds to the Gaussian term of $\Delta V_i^{\mathrm{bias}}$. In order to calculate these quantities, we first need to calculate $V_i^G(\mathrm{masked})$ and $V_i^G(\mathrm{unmasked})$. For this purpose, we measure the following three quantities from 1000 masked ray-tracing maps:

$$\mu = \langle \mathcal{K} \rangle, \ \sigma_0^2 = \langle \mathcal{K}^2 \rangle - \mu^2, \ \sigma_1^2 = \langle |\nabla \mathcal{K}|^2 \rangle. \tag{20}$$

The same quantities are measured also for the unmasked lensing maps. We can then estimate $V_i^G(\mathrm{masked})$ and $V_i^G(\mathrm{unmasked})$ using these quantities and Eq. (6)-(8). For the Gaussian terms, we also consider the correction of the finite binning effect pointed out by Lim & Simon (2012). The correction is needed because the threshold ν to calculate the MFs V_1 and V_2 is not continuous but discrete with some finite width. We calculate the correction by integrating the analytic formula (Eq. (7),(8)) for finite binning width (see Lim & Simon (2012) for details). We then estimate $V_i(\mathrm{masked})$ and $V_i(\mathrm{unmasked})$ from masked and unmasked maps directly. Figure 4 shows the various non-Gaussian contributions (Eq. (16)-(19)) calculated directly from 1000 masked ray-tracing maps. We find that $\Delta V_i^{\mathrm{bias}}$ is comparable to $\Delta V_i^{\mathrm{gravity}}$ in the ray-tracing maps. The mask bias $\Delta V_i^{\mathrm{bias}}$ contributes significantly to the observed non-Gaussianity $\Delta V_i^{\mathrm{obs}}$. Note also that $\Delta V_i^{\mathrm{bias,G}}$ is sub-dominant although not negligible for V_1 and V_2. Clearly the mask bias can be a significant contaminant for cosmological parameter estimation using the lensing MFs. In the following, we include the bias effect when comparing simulation data and observations.

4.3. Application to Subaru Suprime-Cam data

It is important to test whether we can extract cosmological information from masked noisy shear data using the lensing MFs. To this end, we use available Subaru Suprime-Cam data. We analyze the observed weak lensing map by using the statistics derived from a large set of ray-tracing simulations. We include observational effects directly in our simulations, i.e., mask regions and shape noises as described in section 3.2. Figure 5 compares the lensing MFs for the Subaru data and those calculated for the ray-tracing simulations. We plot the MFs V_0, V_1, V_2 in the top panels. In the bottom panels, the thick error bars show the cosmic variance of lensing MFs estimated from our 1000 simulated maps, whereas the thin error bars are the sum of the cosmic variance and the statistical error. We estimate the statistical error from 1000 randomized realizations, in which the ellipticity of each source galaxy is rotated randomly. The statistical error is approximately ~ 1.5 times the cosmic variance for each bin. In order to quantify the consistency of our results, we perform a so-called chi-square analysis. We compute the χ^2 statistics for the observed lensing MFs,

$$\chi^2 = (d_i - m_i)\boldsymbol{C}^{-1}(d_j - m_j) \tag{21}$$

where d_i is the lensing MFs in i-th bin for observation, m_i is the theoretical model, and $\boldsymbol{C}$ is the covariance matrix of lensing MFs including the cosmic variance and the statistical error. The cosmic variance are estimated from 1000 ray-tracing simulations, and the statistical error are computed from 1000 randomized galaxy catalogues. We estimate m_i by averaging the MFs over 1000 ray-tracing simulations. We use 10 bins in the range of $x = [-3, 3]$ for each MF. For the binning, we have a sufficient number of simulations to estimate the covariance matrix of the lensing MFs. The resulting value of χ^2 per number of freedoms is $\chi^2/n_{\rm dof} = 3.35/10, 9.69/10, 12.8/10$ and $29.6/30$ for V_0, V_1, V_2 and all the MFs. The analysis includes the cosmic variance and the statistical error as well as the effect of mask. We conclude that the observed lensing MFs are consistent with the standard ΛCDM cosmology.

4.4. Impact of Masking On Cosmological Parameter Estimation

We study cosmological information content in the lensing MFs with masks. An important quantity is the cumulative signal-to-noise ratio S/N for lensing MFs, which is defined by

$$(S/N)^2 = \boldsymbol{\mu}^t \boldsymbol{C}^{-1} \boldsymbol{\mu}, \tag{22}$$

where $\boldsymbol{\mu}$ is a data vector which consists of the lensing MFs V_0, V_1 and V_2, and $\boldsymbol{C}$ is the covariance matrix. In order to calculate $(S/N)^2$, we construct the data vector from a set of lensing MFs as

$$\{\mu_i\} = \{V_0(x_1), ..., V_0(x_{10}), V_1(x_1), ..., V_1(x_{10}), V_2(x_1), ..., V_2(x_{10})\}, \tag{23}$$

where $x_i(\mathcal{K}_i - \langle\mathcal{K}\rangle)/\sigma_0$ is the binned normalized lensing field.
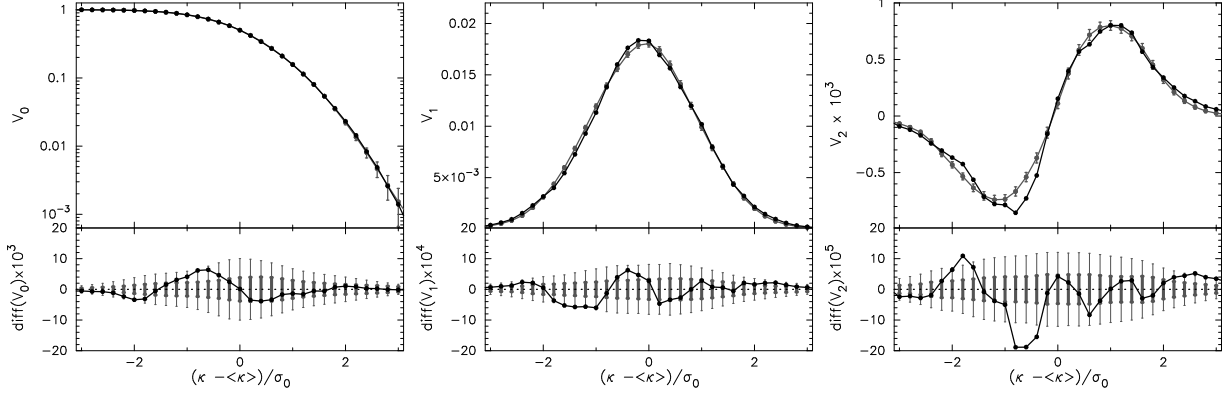
Fig. 5.— We compare the observed MFs with those from cosmological ray-tracing simulations. In the upper panels, the black line shows the observed lensing MFs and the gray one indicates the simulation results. The gray error bars show the cosmic variance obtained from 1000 ray-tracing simulations. In the lower panels, the black line shows the difference between the obtained MFs and the simulation results. The thin error bars are the sum of the cosmic variance and the statistical error while the thick error bars indicate only the cosmic variance. The statistical errors are estimated from 1000 randomized galaxy catalogues.

Figure 6 shows the cumulative signal-to-noise ratio S/N as a function of x_i. Clearly the information content is reduced by a factor of two in the case with mask. The degradation is explained by the reduced effective area. The solid line shows S/N by scaling $\boldsymbol{C}^{-1}$ with the effective survey area. It closely matches the S/N calculated directly from the masked maps. For a Gaussian random field, we expect that the variance of MFs should be inversely proportional to the effective survey area (e.g. Winitzki & Kosowsky 1998; Wang et al. 2009). The result shown in Figure 6 suggests that the effective survey area mainly determines how much cosmological information we can gain from weak lensing MFs.

Let us further quantify the overall impact of bias of the lensing MFs. We perform the following simple analysis to investigate the effect of the mask bias on cosmological parameter estimation. For each realization r of our simulations, we calculate the χ^2 value as follows,

$$\chi^2(r) = (\mu_i(r) - \mu_i^{\text{theory}})\boldsymbol{C}^{-1}(\mu_j(r) - \mu_j^{\text{theory}}), \tag{24}$$

where $\mu_i(r)$ is the estimated lensing MFs from each realization r and μ_i^{theory} is the theoretical template for a given cosmology. In practice, we assume that μ_i^{theory} is the average over our 1000 ray-tracing simulations with or without masks. The lensing MFs $\mu_i(r)$ are estimated for each masked map, and then we use the covariance matrices of the MFs obtained from a total of 1000 masked maps. If $\mu_i(r)$ follows the Gaussian distribution, the distribution of $\chi^2(r)$ should follow a genuine chi-square distribution. We can then clearly see the impact of bias due to masking on cosmological constraints by comparing the resulting distribution of $\chi^2(r)$ for μ_i^{theory} estimated from
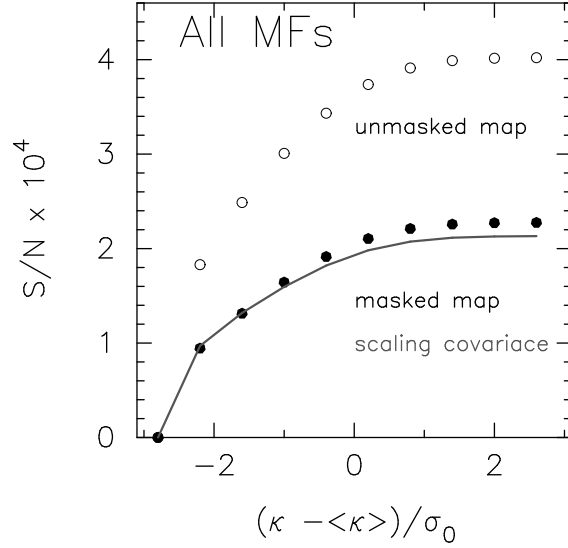
Fig. 6.— The cumulative signal-to-noise ratio for the weak lensing MFs. The horizontal axis represents the maximum value of binned lensing field used in the calculation of S/N. The open circles are the S/N for unmasked 'clean' lensing maps whereas the black points are for masked maps. The solid line shows S/N obtained by scaling the covariance matrices of MFs with the effective survey area. We adopt the mask regions used for the Subaru Suprime-Cam data (see Figure 1).

unmasked maps.

Figure 7 shows the resulting distribution of $\chi^2(r)$ for our 1000 masked ray-tracing simulations. The black histogram is the probability of $\chi^2(r)$ for the corresponding model using the average MFs over the masked maps whereas the gray one is for the unmasked maps. The thick solid line is a genuine chi-square distribution with 30 degrees of freedom, and the dashed line indicates the one-sigma region for the χ^2 values. We find an excellent agreement between the thin histogram and the solid line. This means that the binned lensing MFs $\mu_i(r)$ can be described well by a Gaussian distribution. Interestingly, most of the resulting $\chi^2(r)$ without mask lie outside one sigma regions. When we do not take account of bias due to mask regions, 55.3%, 59.4%, 74.9% and 85.4% of the realizations lies outside one sigma regions of the chi-square values for V_0, V_1, V_2 and all MFs. We conclude that the bias of lensing MFs due to mask regions can crucially compromise cosmological parameter estimation.
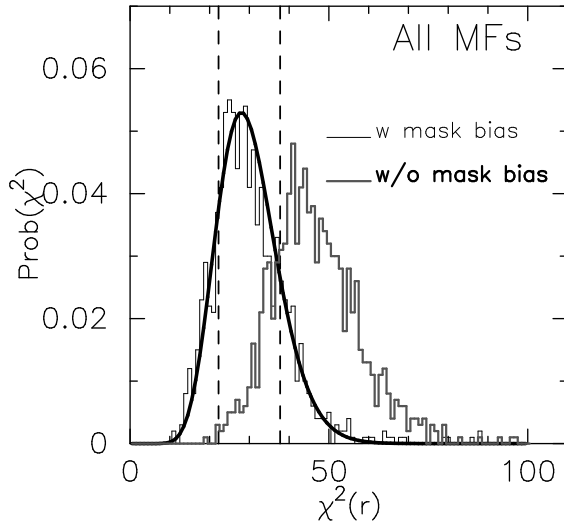
Fig. 7.— We compare the distribution of $\chi^2(r)$ for μ_i^{theory} evaluated for 1000 masked maps (black histogram) with that for μ_i^{theory} evaluated for 1000 unmasked maps. The thick solid lines is a genuine chi-square distribution with 30 degrees of freedom, and dashed line represents the one sigma region.

5. SUMMARY AND CONCLUSION

We have used a large number of numerical simulations to examine how mask regions affect the lensing MFs by adopting the actual sky-mask used for a Subaru observation. We have then compared the observed lensing MFs with the results of cosmological simulations to address whether the observed MFs are consistent with the standard cosmological model.

The weak lensing MFs are affected by the lack of cosmic shear data due mostly to foreground contamination. The expected values of the MFs are biased and the variance is increased even for a Gaussian convergence field. The bias corresponds to about 5 percent differences of the power spectral amplitudes. The bias is induced for the following reasons: (i) masked regions effectively reduce the number of sampling Fourier modes of cosmic shear and (ii) masked regions introduce scatter of variance of the reconstructed weak lensing mass field for each field of view. The former can be corrected analytically as shown in Appendix A, while numerical simulations are needed to study the latter effect. We have used 1000 ray-tracing simulations with mask regions and realistic shape noises, to show that the non-Gaussianities detected by the MFs do not solely come from gravity induced non-Gaussianities. Masked regions significantly contaminate the *pure* gravitational signals.

We have calculated the lensing MFs to the observed weak lensing shear map obtained from a Subaru Suprime-Cam imaging survey. Our analysis include, in addition to the cosmic variance, the statistical error estimated from 1000 randomized galaxy catalogues. The resulting $\chi^2/n_{\mathrm{dof}} =$ 29.6/30 for all the MFs suggests that the observed MFs are consistent with the adopted standard

ΛCDM cosmology.

We also perform simple analysis to examine the impact of mask regions on cosmological parameter estimation. From the cumulative signal-to-noise ratio for the lensing MFs, we have found that the cosmological information content in the MFs can be largely determined by the effective survey area. By studying the resulting distribution of χ^2 value for simulated maps with masks, we can characterize how the "mask bias" of the MFs affects cosmological constraints. We have shown that most of the resulting χ^2 values are found outside the expected one sigma region, when the mask is not considered. Clearly the mask bias compromise significantly the cosmological parameter estimation.

Finally, we address the ability of the lensing MFs to constrain cosmological models. By assuming a simple scaling of the covariance matrix of MFs by survey area, we can reduce the error of MFs in each threshold bin by a factor of ~ 20 (100) for upcoming weak lensing surveys with a 1000 (20000) deg^2 survey area. In the case of a 1000 deg^2 survey, the error in each bin is translated to a ~ 5 percent difference in σ_8. Similarly, for a LSST-like survey with a 20000 deg^2 area, the error in each bin is as small as ~ 0.5 percent in σ_8. The lensing MFs are a promising method for cosmology even with mask regions. It is important to model the effect of mask accurately in order to make the best use of lensing MFs for cosmological constraints. A simplest way would be to use directly the observed mask on ray-tracing simulations as we have done in the present paper. We will need such ray-tracing simulations covering a wide area of more than a thousand square degrees for lensing MFs in upcoming wider surveys.

Further extensive studies are needed in order to devise a way to extract *pure* cosmological information from the lensing MFs. It is important to study how much systematic non-Gaussianities are introduced by, for example, source galaxy clustering (e.g. Bernardeau 1998), source-lens clustering (e.g. Hamana et al. 2002), the intrinsic alignment (e.g. Hirata & Seljak 2004), and inhomogeneous ellipiticity noises due to inhomogeneous surface number density of sources (Shirasaki et al., in preparation). The upcoming wide-field surveys will provide highly-resolved lensing maps but with complicated masked regions. Our study in the present paper may be useful to properly analyze the data and to accurately extract cosmological information from them.

REFERENCES

Bernardeau, F. 1998, A&A, 338, 375

Bertin, E. 2006, in Astronomical Society of the Pacific Conference Series, Vol. 351, Astronomical Data Analysis Software and Systems XV, ed. C. Gabriel, C. Arviset, D. Ponz, & S. Enrique, 112

Bertin, E., & Arnouts, S. 1996, A&AS, 117, 393

Bertin, E., Mellier, Y., Radovich, M., et al. 2002, in Astronomical Society of the Pacific Conference Series, Vol. 281, Astronomical Data Analysis Software and Systems XI, ed. D. A. Bohlender, D. Durand, & T. H. Handley, 228

Bolzonella, M., Miralles, J.-M., & Pelló, R. 2000, A&A, 363, 476

Erben, T., Van Waerbeke, L., Bertin, E., Mellier, Y., & Schneider, P. 2001, A&A, 366, 717

Hamana, T., Colombi, S. T., Thion, A., et al. 2002, MNRAS, 330, 365

Hamana, T., & Mellier, Y. 2001, MNRAS, 327, 169

Hamana, T., Oguri, M., Shirasaki, M., & Sato, M. 2012, MNRAS, 425, 2287

Hamana, T., Takada, M., & Yoshida, N. 2004, MNRAS, 350, 893

Hikage, C., Matsubara, T., Coles, P., et al. 2008, MNRAS, 389, 1439

Hikage, C., Takada, M., Hamana, T., & Spergel, D. 2011, MNRAS, 412, 65

Hirata, C., & Seljak, U. 2003, MNRAS, 343, 459

Hirata, C. M., & Seljak, U. 2004, Phys. Rev. D, 70, 063526

Hoekstra, H., Franx, M., Kuijken, K., & Squires, G. 1998, ApJ, 504, 636

Huterer, D., Takada, M., Bernstein, G., & Jain, B. 2006, MNRAS, 366, 101

Kaiser, N. 2000, ApJ, 537, 555

Kaiser, N., Squires, G., & Broadhurst, T. 1995, ApJ, 449, 460

Komatsu, E., Smith, K. M., Dunkley, J., et al. 2011, ApJS, 192, 18

Kratochvil, J. M., Lim, E. A., Wang, S., et al. 2012, Phys. Rev. D, 85, 103513

Lim, E. A., & Simon, D. 2012, J. Cosmology Astropart. Phys., 1, 48

Luppino, G. A., & Kaiser, N. 1997, ApJ, 475, 20

Matsubara, T., & Jain, B. 2001, ApJ, 552, L89

Oguri, M., Bayliss, M. B., Dahle, H., et al. 2012, MNRAS, 420, 3213

Planck Collaboration, Ade, P. A. R., Aghanim, N., et al. 2013, ArXiv e-prints

Reid, B. A., Percival, W. J., Eisenstein, D. J., et al. 2010, MNRAS, 404, 60

Sato, J., Takada, M., Jing, Y. P., & Futamase, T. 2001, ApJ, 551, L5

Sato, M., Hamana, T., Takahashi, R., et al. 2009, ApJ, 701, 945

Shirasaki, M., Yoshida, N., Hamana, T., & Nishimichi, T. 2012, ApJ, 760, 45

Smith, R. E., Peacock, J. A., Jenkins, A., et al. 2003, MNRAS, 341, 1311

Spergel, D. N., Bean, R., Doré, O., et al. 2007, ApJS, 170, 377

Tegmark, M., Eisenstein, D. J., Strauss, M. A., et al. 2006, Phys. Rev. D, 74, 123507

Tomita, H. 1986, Progress of Theoretical Physics, 76, 952

Wang, S., Haiman, Z., & May, M. 2009, ApJ, 691, 547

White, M., & Hu, W. 2000, ApJ, 537, 1

Winitzki, S., & Kosowsky, A. 1998, New A, 3, 75

A. EFFECT OF MASKS ON VARIANCE OF SMOOTHED CONVERGENCE FIELD

Here, we summarize the effect of masked regions on the variance of a smoothed convergence field $\mathcal{K}$. When there are masked regions in a survey area, one needs to follow a special procedure in order to construct a smoothed convergence field. Let us define the masked region $\mathcal{M}_s(\boldsymbol{\theta})$ in a survey area as

$$\mathcal{M}_s(\boldsymbol{\theta}) = \begin{cases} 1 & \text{where } \boldsymbol{\theta} \text{ lies in data region} \\ 0 & \text{otherwise.} \end{cases} \tag{A1}$$

When the area with mask $\mathcal{M}_s(\boldsymbol{\theta})$ is smoothed, there are ill-defined pixels due to the convolution between $\mathcal{M}_s$ and a filter function for smoothing $U(\boldsymbol{\theta})$. We need to discard the ill-defined pixels to do statistical analyses. We therefore paste a new mask $\mathcal{M}_1(\boldsymbol{\theta})$ so that we can mask the ill-defined pixels as well. We then get

$$\mathcal{K}^{\mathrm{obs}}(\boldsymbol{\theta}) \;=\; \mathcal{M}_1(\boldsymbol{\theta})\mathcal{K}_1(\boldsymbol{\theta}), \tag{A2}$$

where

$$\mathcal{K}_1(\boldsymbol{\theta}) \;=\; \int \mathrm{d}^2\phi\, U(\boldsymbol{\theta} - \boldsymbol{\phi})\mathcal{M}_s(\boldsymbol{\phi})\kappa(\boldsymbol{\phi}). \tag{A3}$$

The variance of the smoothed field is given by

$$\begin{aligned}
\sigma_0^2 \;&=\; \frac{1}{S} \int \mathrm{d}^2\theta \langle \mathcal{K}^{\mathrm{obs}}(\boldsymbol{\theta})^2 \rangle \\
&=\; \frac{1}{S} \int \mathrm{d}^2\theta \mathcal{M}_1(\boldsymbol{\theta}) \langle \mathcal{K}_1(\boldsymbol{\theta})^2 \rangle \\
&=\; \frac{1}{S} \int \mathrm{d}^2\theta \mathcal{M}_1(\boldsymbol{\theta}) \int \frac{\mathrm{d}^2\ell}{(2\pi)^2} \frac{\mathrm{d}^2\ell'}{(2\pi)^2} \langle \mathcal{K}_1(\boldsymbol{\ell})\mathcal{K}_1^*(\boldsymbol{\ell}') \rangle \exp\left(i(\boldsymbol{\ell} - \boldsymbol{\ell}') \cdot \boldsymbol{\theta} \right) \\
&=\; \frac{1}{S} \int \frac{\mathrm{d}^2\ell}{(2\pi)^2} \frac{\mathrm{d}^2\ell'}{(2\pi)^2} \mathcal{M}_1(\boldsymbol{\ell} - \boldsymbol{\ell}') \langle \mathcal{K}_1(\boldsymbol{\ell})\mathcal{K}_1^*(\boldsymbol{\ell}') \rangle,
\end{aligned} \tag{A4}$$

where we use the relation $\mathcal{M}_1(\boldsymbol{\theta})^2 = \mathcal{M}_1(\boldsymbol{\theta})$. The fourier mode of $\mathcal{K}_1$ is given by

$$\begin{aligned}
\mathcal{K}_1(\boldsymbol{\ell}) \;&=\; \int \mathrm{d}^2\theta \mathrm{d}^2\phi\, U(\boldsymbol{\theta} - \boldsymbol{\phi})\mathcal{M}_s(\boldsymbol{\phi})\kappa(\boldsymbol{\phi}) \exp\left(i\boldsymbol{\ell} \cdot \boldsymbol{\theta} \right) \\
&=\; U(\boldsymbol{\ell}) \int \frac{\mathrm{d}^2\ell'}{(2\pi)^2} \mathcal{M}_s(\boldsymbol{\ell}')\kappa(\boldsymbol{\ell} - \boldsymbol{\ell}'), \\
\langle \mathcal{K}_1(\boldsymbol{\ell})\mathcal{K}_1^*(\boldsymbol{\ell}') \rangle \;&=\; U(\boldsymbol{\ell})U^*(\boldsymbol{\ell}') \int \frac{\mathrm{d}^2\ell_1}{(2\pi)^2} \frac{\mathrm{d}^2\ell_1'}{(2\pi)^2} \mathcal{M}_s(\boldsymbol{\ell}_1)\mathcal{M}_s^*(\boldsymbol{\ell}_1') \langle \kappa(\boldsymbol{\ell} - \boldsymbol{\ell}_1)\kappa^*(\boldsymbol{\ell}' - \boldsymbol{\ell}_1') \rangle \\
&=\; U(\boldsymbol{\ell})U^*(\boldsymbol{\ell}') \int \frac{\mathrm{d}^2\ell_1}{(2\pi)^2} \frac{\mathrm{d}^2\ell_1'}{(2\pi)^2} \mathcal{M}_s(\boldsymbol{\ell}_s)\mathcal{M}_s^*(\boldsymbol{\ell}_1')(2\pi)^2\delta^{(2)}(\boldsymbol{\ell} - \boldsymbol{\ell}_1 - \boldsymbol{\ell}' + \boldsymbol{\ell}_1')P_\kappa(|\boldsymbol{\ell} - \boldsymbol{\ell}_1|) \\
&=\; U(\boldsymbol{\ell})U^*(\boldsymbol{\ell}') \int \frac{\mathrm{d}^2\ell_1}{(2\pi)^2} \mathcal{M}_s(\boldsymbol{\ell}_1)\mathcal{M}_s^*(\boldsymbol{\ell}_1 + \boldsymbol{\ell}' - \boldsymbol{\ell})P_\kappa(|\boldsymbol{\ell} - \boldsymbol{\ell}_1|)
\end{aligned} \tag{A5}$$

In the following, we assume that $\mathcal{M}_1(\boldsymbol{\theta})$ is large enough to cover the ill-defined pixels due to smoothing (with a fliter function) of the original mask region $\mathcal{M}_s(\boldsymbol{\theta})$. This means that, with $\mathcal{M}_1(\boldsymbol{\theta})$, there remains only *clean* regions where the smoothed convergence is not affected by the original mask regions $\mathcal{M}_s(\boldsymbol{\theta})$. In this case,

$$\mathcal{K}^{\mathrm{obs}}(\boldsymbol{\theta}) \simeq \mathcal{M}_1(\boldsymbol{\theta}) \int \mathrm{d}^2\phi\, U(\boldsymbol{\theta} - \boldsymbol{\phi})\kappa(\boldsymbol{\phi}). \tag{A6}$$

The fourier mode of $\mathcal{K}^{\mathrm{obs}}$ can then be given by

$$
\begin{aligned}
\mathcal{K}^{\mathrm{obs}}(\boldsymbol{\ell}) &= \int \mathrm{d}^2\theta\, \mathcal{K}^{\mathrm{obs}}(\boldsymbol{\theta}) \exp\left(i\boldsymbol{\ell} \cdot \boldsymbol{\theta}\right) \\
&\simeq \int \mathrm{d}^2\theta\, \mathcal{M}_1(\boldsymbol{\theta}) \int \mathrm{d}^2\phi\, U(\boldsymbol{\theta} - \boldsymbol{\phi})\kappa(\boldsymbol{\phi}) \exp\left(i\boldsymbol{\ell} \cdot \boldsymbol{\theta}\right) \\
&= \int \mathrm{d}^2\theta' \mathrm{d}^2\theta \mathrm{d}^2\phi\, \mathcal{M}_1(\boldsymbol{\theta}')\delta^{(2)}(\boldsymbol{\theta} - \boldsymbol{\theta}')U(\boldsymbol{\theta} - \boldsymbol{\phi})\kappa(\boldsymbol{\phi}) \exp\left(i\boldsymbol{\ell} \cdot \boldsymbol{\theta}\right) \\
&= \int \frac{\mathrm{d}^2\ell'}{(2\pi)^2} \int \mathrm{d}^2\theta' \mathrm{d}^2\theta \mathrm{d}^2\phi\, \mathcal{M}_1(\boldsymbol{\theta}')U(\boldsymbol{\theta} - \boldsymbol{\phi})\kappa(\boldsymbol{\phi}) \exp\left(i\boldsymbol{\ell} \cdot \boldsymbol{\theta}\right) \exp\left(-i\boldsymbol{\ell}' \cdot (\boldsymbol{\theta} - \boldsymbol{\theta}')\right) \\
&= \int \frac{\mathrm{d}^2\ell'}{(2\pi)^2} \mathcal{M}_1(\boldsymbol{\ell}') \int \mathrm{d}^2\theta \mathrm{d}^2\phi\, U(\boldsymbol{\theta} - \boldsymbol{\phi})\kappa(\boldsymbol{\phi}) \exp\left(i(\boldsymbol{\ell} - \boldsymbol{\ell}') \cdot \boldsymbol{\theta}\right) \\
&= \int \frac{\mathrm{d}^2\ell'}{(2\pi)^2} \mathcal{M}_1(\boldsymbol{\ell}')U(\boldsymbol{\ell} - \boldsymbol{\ell}')\kappa(\boldsymbol{\ell} - \boldsymbol{\ell}'). \tag{A7}
\end{aligned}
$$

The variance of the smoothed convergence field is calculated as

$$
\begin{aligned}
\sigma_0^2 &= \frac{1}{S} \int \mathrm{d}^2\theta \langle \mathcal{K}^{\mathrm{obs}}(\boldsymbol{\theta})^2 \rangle \\
&= \frac{1}{S} \int \mathrm{d}^2\theta \int \frac{\mathrm{d}^2\ell}{(2\pi)^2} \frac{\mathrm{d}^2\ell'}{(2\pi)^2} \langle \mathcal{K}^{\mathrm{obs}}(\boldsymbol{\ell}) \mathcal{K}^{\mathrm{obs}}(\boldsymbol{\ell}') \rangle \exp\left(-i(\boldsymbol{\ell} - \boldsymbol{\ell}') \cdot \boldsymbol{\theta}\right) \\
&= \frac{1}{S} \int \frac{\mathrm{d}^2\ell}{(2\pi)^2} \langle \mathcal{K}^{\mathrm{obs}}(\boldsymbol{\ell})(\mathcal{K}^{\mathrm{obs}})^*(\boldsymbol{\ell}) \rangle, \tag{A8}
\end{aligned}
$$

where the ensemble average of the fourier mode is

$$
\begin{aligned}
\langle \mathcal{K}^{\mathrm{obs}}(\boldsymbol{\ell})(\mathcal{K}^{\mathrm{obs}})^*(\boldsymbol{\ell}') \rangle &\simeq \int \frac{\mathrm{d}^2\ell_1}{(2\pi)^2} \frac{\mathrm{d}^2\ell_1'}{(2\pi)^2} \mathcal{M}_1(\boldsymbol{\ell}_1)\mathcal{M}_1^*(\boldsymbol{\ell}_1')U(\boldsymbol{\ell} - \boldsymbol{\ell}_1)U^*(\boldsymbol{\ell}' - \boldsymbol{\ell}_1') \\
&\qquad \times \langle \kappa(\boldsymbol{\ell} - \boldsymbol{\ell}_1)\kappa^*(\boldsymbol{\ell}' - \boldsymbol{\ell}_1') \rangle \\
&= \int \frac{\mathrm{d}^2\ell_1}{(2\pi)^2} \frac{\mathrm{d}^2\ell_1'}{(2\pi)^2} \mathcal{M}_1(\boldsymbol{\ell}_1)\mathcal{M}_1^*(\boldsymbol{\ell}_1')U(\boldsymbol{\ell} - \boldsymbol{\ell}_1)U^*(\boldsymbol{\ell}' - \boldsymbol{\ell}_1') \\
&\qquad \times (2\pi)^2 P_\kappa(|\boldsymbol{\ell} - \boldsymbol{\ell}_1|)\delta^{(2)}(\boldsymbol{\ell} - \boldsymbol{\ell}_1 - \boldsymbol{\ell}' + \boldsymbol{\ell}_1') \\
&= \int \frac{\mathrm{d}^2\ell_1}{(2\pi)^2} \mathcal{M}_1(\boldsymbol{\ell}_1)\mathcal{M}_1^*(\boldsymbol{\ell}_1 + \boldsymbol{\ell}' - \boldsymbol{\ell})|U(\boldsymbol{\ell} - \boldsymbol{\ell}_1)|^2 P_\kappa(|\boldsymbol{\ell} - \boldsymbol{\ell}_1|). \tag{A9}
\end{aligned}
$$

We have checked the validity of Eq.(A6) by using 1000 Gaussian simulations. They are the same set of simulations as in 3.2. For each Gaussian simulation, we paste the observed mask region
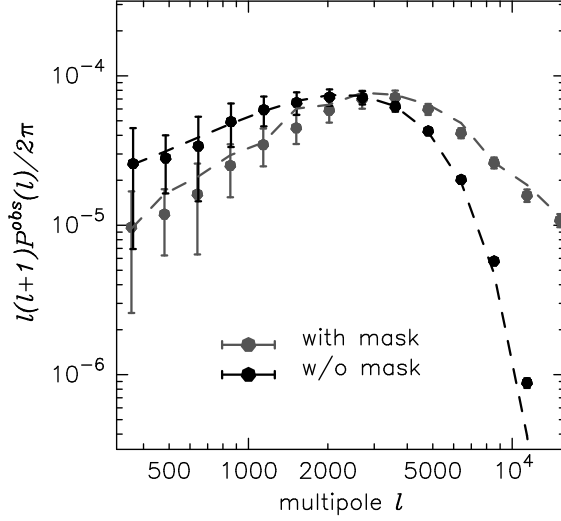
Fig. 8.— We test the validity of Eq.(A6). The gray points with error bars show $P^{\mathrm{obs}}(\ell)$ obtained from 1000 Gaussian maps with mask $\mathcal{M}_s(\boldsymbol{\theta})$. The gray dashed line is the theoretical prediction of Eq.(A11).The black points with error bars show $P^{\mathrm{obs}}(\ell)$ obtained from 1000 maps without mask. The black dashed line is the input power spectrum smoothed by the Gaussian filter U.

$\mathcal{M}_s(\boldsymbol{\theta})$ from the Subaru Suprime-Cam observation. The map is then smoothed with a Gaussian filter of Eq.(9). The adopted smoothing scale is 1 arcmin. In order to avoid the ill-defined pixels, we paste a new mask $\mathcal{M}_1(\boldsymbol{\theta})$, which is constucted conservatively to cover the regions within 2 times the smoothing scale from the boundary of the original mask $\mathcal{M}_s(\boldsymbol{\theta})$. We then calculate

$$P^{\mathrm{obs}}(\ell) \quad \equiv \quad \langle \mathcal{K}^{\mathrm{obs}}(\boldsymbol{\ell})(\mathcal{K}^{\mathrm{obs}})^*(\boldsymbol{\ell}) \rangle / S. \tag{A10}$$

If $\mathcal{K}^{\mathrm{obs}}$ can be well-approximated by Eq. (A6), this quantity should be given by

$$P^{\mathrm{obs}}(\ell) \quad \simeq \quad \frac{1}{S} \int \frac{\mathrm{d}^2\ell_1}{(2\pi)^2} |\mathcal{M}_1(\boldsymbol{\ell}_1)|^2 |U(\boldsymbol{\ell} - \boldsymbol{\ell}_1)|^2 P_\kappa(|\boldsymbol{\ell} - \boldsymbol{\ell}_1|). \tag{A11}$$

Figure 8 compares Eq. (A6) and Eq. (A11). Clearly Eq. (A6) is an excellent approximation for the observed survey geometry. The ill-defined pixels are efficiently masked by $\mathcal{M}_1(\boldsymbol{\theta})$. We also find the variance σ_0^2 decreases by a factor of $O(5\%)$. This causes the bias of Minkowski Functionals even if the lensing field is Gaussian.